Journal of Magnetic Resonance 337 (2022) 107171

Contents lists available at ScienceDirect

Journal of Magnetic Resonance

journal homepage: www.elsevier.com/locate/jmr

Deuteron rotating frame relaxation for the detection of slow motions in rotating solids

Liliya Vugmeyster [a,*], Dmitry Ostrovsky [b], Alexander Greenwood [c], Riqiang Fu [d]

[a] Department of Chemistry, University of Colorado Denver, Denver, CO 80204, USA
[b] Department of Mathematics, University of Colorado Denver, Denver, CO 80204, USA
[c] Department of Chemistry, University of Cincinnati, Cincinnati, OH 45221-0172, USA
[d] National High Field Magnetic Laboratory, Tallahassee, FL 32310, USA

ARTICLE INFO

Article history:
Received 29 November 2021
Revised 15 February 2022
Accepted 16 February 2022
Available online 19 February 2022

Keywords:
Deuterium NMR
Solid-state NMR
NMR relaxation
Protein dynamics

ABSTRACT

We demonstrate experimental and computational approaches for measuring ^{2}H rotating frame NMR relaxation for solid samples under magic angle spinning (MAS) conditions. The relaxation properties of the deuterium spin-1 system are dominated by the reorientation of the anisotropic quadrupolar tensors, with the effective quadrupolar coupling constant around 55 kHz for methyl groups. The technique is demonstrated using the model compound dimethyl-sulfone at MAS rates of 10 and 60 kHz as well as for an amyloid fibril sample comprising an amyloid-β (1–40) protein with a selective methyl group labeled in the disordered domain of the fibrils, at an MAS rate of 8 kHz. For both systems, the motional parameters fall well within the ranges determined by other techniques, thus validating its feasibility. Experimental and computational factors such as i) the probe's radio frequency inhomogeneity profiles, ii) rotary resonances at conditions for which the spin-lock field strength matches the half- or full-integer of the MAS rate, iii) the choice of MAS rates and spin-lock field strengths, and iv) simulations that account for the interconversion of multiple coherences for the spin-1 system under MAS and deviations from the analytical Redfield treatment are thoroughly considered.

1. Introduction

Internal motions in proteins on μs-ms time scale range are essential for multiple biological functions.[1–3] Following solution NMR approaches, relaxation dispersion approaches for proteins in the solid state are in the active stage of development.[2,4–15] Most of the currently developed techniques cover spin ½ nuclei such as ^{15}N, ^{13}C, and ^{1}H.[11,15–17] Rotating frame relaxation ($R_{1\rho}$) experiments in solids have the capacity to probe both the fluctuations of the isotropic chemical shift component and the fluctuations of the anisotropic tensor due to conformational changes.[15] Under magic angle spinning (MAS) conditions, the latter has been shown to modulate the width of rotational resonances.[13,14]

Deuterium relaxation is a sensitive tool for measuring the dynamics in a variety of systems.[18–21] Deuterium is a spin-1 nucleus and its relaxation is governed primarily by the quadrupole interaction.[20] Further, as the typical quadrupolar interaction is of the order of 150–200 kHz, their magnitude is considerably larger than dipolar and chemical shift anisotropy interactions.[20–22] On the one hand, this larger magnitude allows us to focus on the quadrupolar interaction as a major source of relaxation, while neglecting minor dipolar contributions. On the other hand, it requires modifications of established experimental and computational approaches developed for spin ½ nuclei governed by smaller magnitudes of the interactions. ^{15}N and ^{13}C $R_{1\rho}$ studies in the solid state often focus on changes in the isotropic chemical shifts upon conformational changes, similar to solution NMR approaches. In our case, focus is placed on the anisotropic quadrupolar tensor reorientations due to stochastic processes. We previously developed the $R_{1\rho}$ experiment for ^{2}H nuclei under static conditions [23] and applied it to model compounds and amyloid fibril samples.[24–27] In many applications, MAS conditions are desirable for site-specific resolution[2]. For the case of deuterium, site-specificity in multiply labeled samples will require polarization transfer steps to nuclei that offer a larger chemical shift dispersion, such as ^{13}C.[28] Coupling to MAS also offers an advantage of increased signal to noise ratio, as an alternative to static multiple echo acquisition detection. [29]

The goal of this work is to demonstrate experimental and computational approaches for conducting deuterium $R_{1\rho}$

* Corresponding author at: Department of Chemistry, University of Colorado at Denver, 1201 Larimer St, Denver, CO 80204, USA.
E-mail address: liliya.vugmeyster@ucdenver.edu (L. Vugmeyster).

https://doi.org/10.1016/j.jmr.2022.107171
1090-7807/

measurements under MAS conditions. We employ the same systems used to develop static measurements to allow the direct comparison of the results (Fig. 1). Dimethyl-sulfone (DMS-D_6) is a well-studied model compound undergoing 2-site flips around the C_2 symmetry axis (Fig. 1A), which fall into the approximate range of $5{\cdot}10^2$ to $4{\cdot}10^4$ s^{-1} at elevated temperatures between about 45 °C and 85 °C.[9,30–34] As usual with methyl groups, the additional mode of fast methyl jumps at the picosecond time scale narrows the quadrupolar tensor threefold, yielding an effective quadrupolar coupling constant of 55 kHz.[20] The second system is a test of feasibility in proteins, especially in amorphous powder samples. This comprises hydrated amyloid- β fibrils in the threefold symmetric polymorph formed by the A $\beta_{1\text{-}40}$ peptide [35,36] (Fig. 1B). A β fibrils, hallmarks of Alzheimer's disease, exist in multiple morphological forms, of which the 3-fold symmetric polymorph is the more toxic.[36] The disordered N-terminal domain (residues 1–16) has been found to be mobile by multiple studies and has been implicated in the aggregation control of A β.[37–41] The fibrils employed in this work are labeled with deuterium at a single site of the alanine-CD_3 group, located at position 2 of the flexible disordered N-terminal domain. This domain undergoes a complex conformational exchange process, which we have previously characterized by static ^{2}H NMR approaches and ^{2}H CEST under MAS measurements.[24–27] Here, we assess the motions using the on-resonance $R_{1\ \rho}$ relaxation dispersion technique and compare the results with those of previous approaches to cross-validate and assess the limits of applicability of the technique. In addition to the experimental data on DMS and the fibrils, we perform simulations involving a simple two-site exchange model (Fig. 1C) to understand the behavior of the spin-1 system under spin-lock conditions in the presence of coherent time evolution due to MAS.

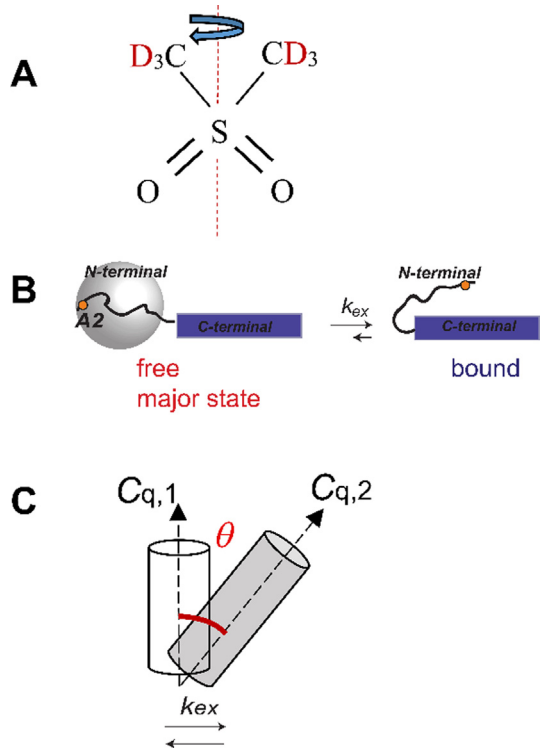

Fig. 1. A) Structure of DMS indicating the 180° flipping motion around the C_2 axis, corresponding to θ = 106°. An additional motional mode of 3-site methyl jumps is a part of the model but is not shown explicitly. B) Slow time scale motional modes of the A2-CD_3 methyl group of the N-terminal domain of hydrated A $\beta_{1\text{-}40}$ fibrils.[27] The disordered N-terminal domain (residues 1–16, curved line) transiently interacts with the structured C-terminal domain (blue rectangle). In the free state, the N-terminal domain undergoes large-scale diffusive motion, as represented by the gray sphere, which is absent in the bound state. The position of the A2 residue is shown as an orange dot. C) Theoretical 2-site exchange model for two axially symmetric tensors with quadrupolar coupling constants denoted by $C_{q,1}$ and $C_{q,2}$ and the jump angle denoted by θ.

2. Experimental

2.1. Materials

DMS-D_6 was purchased from Cambridge Isotope Laboratories, Inc. (MA) and packed as a powder into rotors. The A $\beta_{1\text{-}40}$ fibrils labeled at the A2-CD_3 site were prepared as previously described in the 3-fold symmetric polymorph.[24,27] The monomeric sequence of the A $\beta_{1\text{-}40}$ peptide was D{**A-CD_3**}EFRHDSGYEVHHQKLVFFAEDVGSNKGAIIGLMVGGVV. The lyophilized powder was hydrated to 200% by weight with deuterium-depleted water using direct pipetting and equilibrating at room temperature for 5 days. The hydrated sample was then packed into a 2.5 mm rotor.

2.2. NMR spectroscopy

The $R_{1\ \rho}$ measurements at MAS rates of 8 kHz (fibrils) and 10 kHz (DMS) were taken using a 17.6 T Bruker Avance I spectrometer equipped with a Bruker 2.5 mm HXY probe (College of William and Mary). The measurements at a 60 kHz MAS rate for DMS were taken using a 14.1 T Bruker NEO console spectrometer equipped with a Bruker 1.3 mm HXY probe (NHFML). High-power 90° radio frequency (RF) pulses corresponded to 2 μs. The number of scans acquired was between 12 and 32 at a 10 kHz MAS rate for DMS, 4 and 16 at a 60 kHz MAS rate for DMS, and 1792 and 4096 at an 8 kHz MAS rate for the fibril sample. For spectral processing, the exponential line-broadening function was employed with 100 Hz for DMS at the 10 kHz MAS rate, 10 Hz for DMS at the 60 kHz MAS rate, and 50 Hz for the fibril sample.

2.3. Modeling

The evolution under MAS was modeled using the numerical integration of the Liouville–von Neumann equation (Eq. (SI-5)) with the quadrupolar frequency evolution given by Eq. (SI-4). The time dependence of the Liouvillian matrix was modeled by 20 points equally spaced over a single MAS rotation period. An internal Matlab function for matrix exponentiation was used to approximate the evolution operator over the corresponding time span for each of the 20 points. The matrix of the evolution operator for the full MAS period rotation was then calculated by multiplying by the evolution matrices for the individual time intervals. No approximation involving separation of the coherent and incoherent evolution was made. The sufficiency of 20 time steps was established by confirming the stability of the results after increasing the number of time steps to 100. The evolution matrix for a time period during the spin-lock was obtained by first calculating the evolution matrix for the integer number of rotor periods within the selected time of evolution. The evolution matrix for the integer part was calculated by taking an appropriate power of the evolution matrix for a single rotor period. The evolution matrix during the remaining fractional time of the rotor period is calculated separately and is included as an additional matrix multiplication. The FID evolution was calculated in a likewise manner but with a simplification owing to the possibility of the separation of the transverse coherence evolution for the linear combinations of individual coherences $\widehat{S}_x, \widehat{S}_y, \widehat{J}_x, \widehat{J}_y$ from the rest of the basis listed in Eq. (SI-1) in the absence of the RF field. The time interval for

the individual step for generating FID was taken as the smaller value between 1/20th of the MAS period and the dwell time. The above procedure presents the calculations for an individual crystallite of the solid powder. The powder averaging was performed according to the ZCW scheme.[42,43] We used 1596 crystallite orientations for the DMS calculations and 233 orientations for the fibril simulations.

The simulations of the jump matrices necessary to model the motional mechanisms of Fig. 1 closely followed the procedures outlined in prior work for the cases of the static measurements. In particular, the simulation of the spherical diffusion for the dominant free state of A β fibrils (depicted in Fig. 1B) coupled to the conformational exchange was performed in the following manner. The exchange matrix K_{ij} of Eq. (SI-5) combines components responsible for the isotropic diffusion and the conformational exchange between the free diffuse ion state and the bound state, according to the following scheme:

$$K = \begin{pmatrix} \text{diffusion} & \text{exchange with bound state} \\ \text{exchange with bound state} & \end{pmatrix}$$

The block of the exchange matrix K_{ij} responsible for the diffusion, is represented by nearest neighbor jumps with sites of equal populations distributed (almost) uniformly on the surface of the sphere and with identical exchange rates between the sites, $K_{ij} = k_D$. We used the program DistMesh,[44] which creates the uniform distribution of sites by assuming a linear repulsive force and solving for the equilibrium. The inclusion of $N_D = 192$ sites is sufficient to adequately represent the isotropic diffusion process and leads to the following range of jump angles in the crystal-fixed frame between the sites: 13.7–18.7°. Due to the spin 1 symmetry properties, only the second-order spatial spherical harmonics give rise to the spectral densities. Thus, the second-order eigenfunction of the Smoluchowski diffusion equation encodes the spatial reorientation and the corresponding eigenvalue is related to the diffusion coefficient D as $Dl(l+1) = 6D$. As expected, the simulated eignevalues of K_{ij} appear in groups of $2l+1$, corresponding to the eigenvectors with the angular momentum l of the continuous limit of the diffusion equation. The five eigenvalues λ_2 corresponding to $l = 2$ are then averaged to obtain the numerical value of D. This establishes the correspondence between D and k_D as $k_D = 6D/\langle\lambda_2\rangle$. To include the exchange process, one additional site with a fixed angular position corresponding to the bound state was added to yield a total of $N_D + 1$ sites. The exchange was modeled by jumps between every site describing the spherical diffusion and the bound-state site with an arbitrary fixed angular position with the rate k_{ex}/N_D. Modeled in this fashion, the relative tensor orientation in the free and bound states is averaged over the uniform spherical distribution. Simulated decays utilized time points identical to those used in the experiment. The simulations were performed on an x86_64 Intel Xenon Silver dual core CPU node. Each node had 16 Intel Xenon Silver dual core CPUs and 16 GB of memory.

The RF inhomogeneity profiles for both probes (depicted in Fig. 2B) can be approximated using discrete profiles around each selected RF strength value.[45] The chosen discretization coarseness depends on a number of factors such as proximity to the rotary resonances requiring a finer grid and the overall time of each simulation, which limits the number of points for computationally intensive motional models. Once the grid is determined, partially relaxed spectra are calculated for each RF value of the grid and the weighted average is constructed with the appropriate weights of the distribution profile to obtain the final simulated spectrum at each $\langle\omega_{RF}\rangle$ value. For DMS, a grid of 0.1 kHz was used, yielding 12–50 discretization points. For the computationally intense simulations of the fibrils, for each simulated average $\langle\omega_{RF}\rangle$ value, a five-point grid was used. These points corresponded to the RF values at 0.25, 0.5, 0.75, 1, and 1.25 multiples of the average frequency with the corresponding relative weights of 0.065, 0.097, 0.103, 0.236, and 0.499 for the 2.5 mm probe profile.

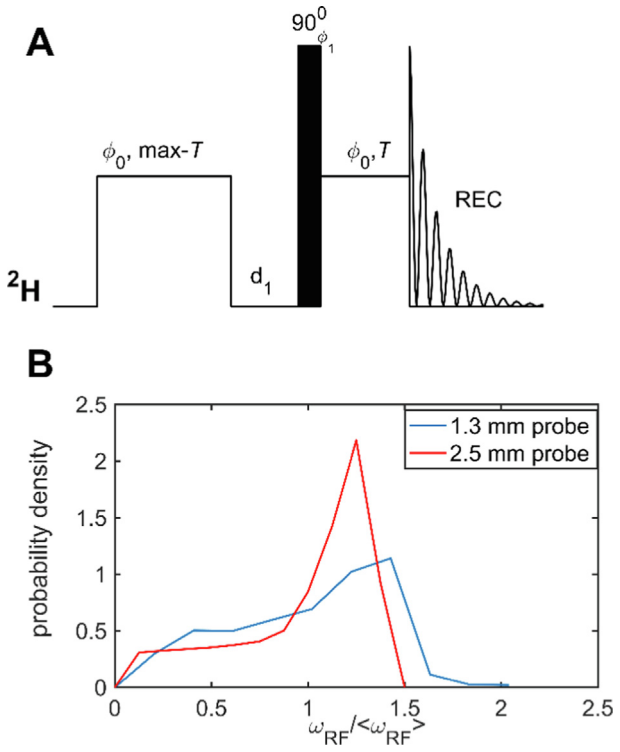

Fig. 2. A) Pulse sequence for the ^{2}H solid-state $R_{1\rho}$ measurements under MAS. The heat compensation block (max-T) is followed by the inter-scan delay d_1 and the preparation 90° pulse, followed by a variable spin-lock delay (T), directly proceeded by the FID collection. The phase cycle corresponds to $\phi_0 = x$, $\phi_1 = -y,y$, and receiver = $-y,y$. The duration of d_1 varied between 1 and 3.5 s to maintain a constant temperature. B) Inhomogeneity profiles of the two probes as a function of $\omega_{RF}/\langle\omega_{RF}\rangle$ obtained for the weighted averages $\langle\omega_{RF}\rangle$ in the range of 2.8–40 kHz for the 1.3 mm Bruker HXY probe using DMS-D_6 (at 14.1 T) and 5–31 kHz for the 2.5 mm Bruker HXY probe using hexamethylbenzene-D_{18} (at 17.6 T).[45]

3. Results and discussion

3.1. The $R_{1\rho}$ experiment

The $R_{1\rho}$ measurements were performed according to the scheme in Fig. 2A, which utilizes a heat compensation block that ensures the same amount of heating for all the relaxation delays. Transverse magnetization was created by a high-power 90° pulse, followed by the spin-lock evolution and detection periods. The phase cycle was analogous to that of Vega.[46] The inter-scan delay d_1 was set between 1 and 3.5 s to minimize the RF-induced heating for all the spin-lock field strengths and maintain a constant temperature among them. As DMS longitudinal relaxation times (T_1) are very sensitive to temperatures in the 40–85 °C range, we used them as an internal calibration standard to obtain the actual temperature in the sample.[23] $T1$ values in the presence of a "dummy" spin-lock heat compensation block were also used to assess the inter-scan delay necessary to keep the effective T_1, and thus temperature, the same across all the spin-lock field strengths.

The same optimized parameters were applied to the fibril sample, assuming as a first approximation that the RF induced-heating would be relatively similar in the two samples.

As will be elaborated below, the choices of MAS rates and spin-lock powers depend on multiple factors such as the magnitude of the quadrupolar tensor of the system and tolerance to the RF-induced heating of the probe and sample. For each spin-lock field strength, magnetization decay curves need to be sampled with a sufficient number of points to capture the details of the decay. The RF inhomogeneity factor can be rather significant and must be taken into account for quantitative interpretation of the results. We have previously assessed the inhomogeneity of the profiles of the two probes (Bruker 2.5 mm HXY and Bruker 1.3 mm HXY probes) using ^{2}H nutation experiments on either DMS or hexamethyl-benzene-D_{18}. As the latter has a narrower tensor [47], it is more suitable for calibrations at slow MAS conditions. The profiles (Fig. 2B) are approximately proportional to the average RF frequency (Fig. S1) and thus can be plotted as a function of $\omega_{RF}/\langle\omega_{RF}\rangle$, in which $\langle\omega_{RF}\rangle$ is the weighted average over the distribution. The profiles' shape and width, with relatively long low-field tails and a sharper high-field edge, are consistent with studies of ^{13}C nuclei. [48] We report $\langle\omega_{RF}\rangle$ as the effective RF field strength in all the data below.

3.2. Qualitative insights from the 2-site jump simulations

Rotating frame relaxation under MAS for spin ½ nuclei involved in heteronuclear and homonuclear dipolar interactions, CSA interactions, and isotropic chemical shift changes has been considered in multiple recent works and reviews.[2,4–15] Most works adopt the Redfield approximation when applicable for ease of interpretation; however, the limitations of the Redfield treatment has been noted in many cases,[2] especially for conditions in the vicinity of rotary resonances at which the spin-lock RF frequency ω_{RF} matches the integer or half-integer multiples of the MAS frequency ω_{MAS}. For the proton–proton homonuclear dipolar case, the Redfield approximation can significantly overestimate relaxation rates, even far from the rotary resonance conditions for large-angle fluctuations and/or strong collision limit as well as in the intermediate motional regime.[12] A large magnitude of quadrupolar tensors compared with dipolar interactions shrink the limit of the validity of the Redfield theory even further for a ^{2}H spin-1 nucleus. In the static case, the limit of its validity is given by the condition that the conformational exchange rate constant k_{ex} is much higher than the typical quadrupolar frequency ω_Q for different crystallite orientations.[23] For DMS methyl groups, the typical value of ω_Q is about $1.3{\cdot}10^5$ rad/s (calculated from $\omega_Q = 2\pi{\cdot}20$ kHz), while the large-angle flip rate constant is in the $0.2–1{\cdot}10^5$ s^{-1} range, thus the Redfield limit does not hold.[23] In the case of MAS, the situation becomes even more complex due to the coherent averaging of the quadrupolar frequency (considered in more detail below).

We thus perform all the subsequent simulations using the full Liouvillian treatment and below we demonstrate the main insight into relaxation behavior according to the 2-site jump model with the parameters of the quadrupolar tensors typical for methyl groups. A summary of the theory is presented in the SI1 and is similar to approaches in previous works.[45 23]

The coherent dephasing of the transverse magnetization for spin-1 nuclei under MAS in the presence of the spin-lock field occurs at the rotary resonance conditions for which $\omega_{RF} = \frac{n}{2}\omega_{MAS}$, where n is an integer (Fig. 3). They arise due to the loss of lock for the transverse coherence $\widehat{S}_x$ at these matching conditions. The situation is analogous to that described for homonuclear dipolar interactions,[12,14,17] with the half-integer rotary resonance referred to as the HORROR condition.[49]

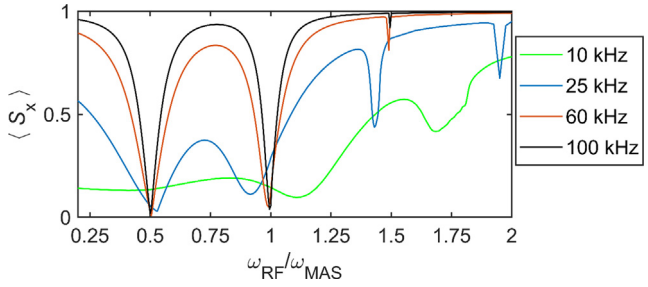

Fig. 3. Mean value of the transverse deuteron $\widehat{S}_x$ coherence over a 5 ms spin-lock period in the absence of motions *vs* ω_{RF}/ω_{MAS} for the four values of ω_{MAS} shown directly in the panel. An axially symmetric tensor with $C_q = 55$ kHz was used with powder averaging over 1596 crystallite orientations and a static magnetic field strength of 17.6 T.

When the value of C_q is greater than the MAS rate, one can expect apparent shifts in these resonance conditions from the above equations (see Fig. 3 and Fig. S2, where the effect is elaborated for individual crystallite orientations). The apparent shift occurs due to presence of coherence oscillations of ω_Q at both the ω_{MAS} and the $2\omega_{MAS}$ frequencies:

$$\omega_Q(t) = \frac{3\pi}{4}C_q\left(\sqrt{2}\sin 2\beta\sin(\omega_{MAS}t+\alpha) - \sin^2\beta\cos(2\omega_{MAS}t+2\alpha)\right) \quad (1)$$

where β and α are the polar and azimuthal angles with respect to the axis of rotation, respectively. For high MAS frequencies with respect to the C_q value, the second- and higher-order effects beyond $n = 2$ are greatly diminished (Fig. 3, black and red lines).

Motions lead to the incoherent contribution of $\widehat{S}_x$ evolution by stochastic changes in the quadrupolar tensor parameters by changing either the magnitude of the quadrupolar coupling constant in different conformational states or the orientation of the tensor, both of which affect the value of ω_Q and thus lead to relaxation. As discussed above, the conventional and simplest treatment of relaxation can be performed according to the Redfield formalism. The Hamiltonian corresponding to the quadrupolar interaction of spin-1 nucleus has the same form as the homonuclear dipolar Hamiltonian for two spins ½, due to the same symmetry. The analytical expression for rotating frame relaxation for the homonuclear case in the presence of MAS has been derived previously [12,17,50]. This expression can be applied to the quadrupolar spin-1 case, at least for an axially symmetric quadrupolar tensor:

$$R_{1\rho} = \frac{3\pi^2}{2}C_q^2\left[\frac{1}{2}(J_0(\omega_{MAS}-2\omega_{RF})+J_0(\omega_{MAS}+2\omega_{RF})) + \frac{1}{4}(J_0(2\omega_{MAS}-2\omega_{RF})+J_0(2\omega_{MAS}+2\omega_{RF})) + \frac{5}{2}J_1(\omega_L)+J_2(2\omega_L)\right] \quad (2)$$

where J_0, J_1, and J_2 are the spectral densities, defined in detail for deuteron nuclei in [20], and ω_L is the Larmor frequency. For static solid powders, the spectral densities depend on the orientation of crystallites in addition to the details of molecular motions. However, in the presence of MAS, a simplified approach is often employed in which orientation dependence is averaged, leading to the same functional form of the spectral densities.[2,50].

For a 2-site exchange model (Fig. 1C) with axially symmetric tensors, these orientation-averaged spectral densities can be calculated from the static spectral densities given in [20,51]

$$J_0(\omega) = J_1(\omega) = J_2(\omega) = \frac{3}{5}p_1p_2\sin^2\theta\frac{kex}{kex^2+\omega^2}$$

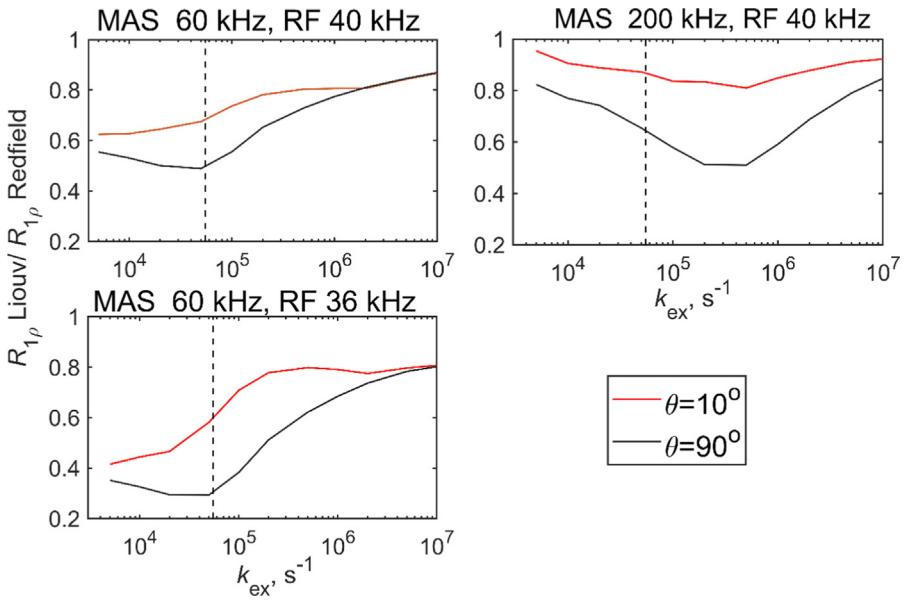

Fig. 4. Ratio of the ^{2}H NMR relaxation rates $R_{1\rho}$ calculated by applying the Liouvillian treatment to the Redfield treatment (Eq. (2)) as a function of k_{ex} for the values of $\omega_{RF}/2\pi$ and $\omega_{MAS}/2\pi$ shown directly in the panels. The 2-site exchange model in Fig. 1C was used with $C_{q,1} = C_{q,2} = 55$ kHz, $p_1 = p_2 = 0.5$, and two values of the jump angle θ. The dotted line indicates the condition $C_q = k_{ex}$.

where p_1 and p_2 are the populations of the two sites, θis the jump angle, and $k_{ex} = k_1 + k_{-1}$ is the sum of the forward and backward jump rate constants. Fig. 4 compares the relaxation rates calculated using either the Redfield approach or the Liouvillian treatment and employing the two-site exchange model with the quadrupolar coupling constant fixed at both exchange sites at 55 kHz, typical of the effective tensor of methyl groups. We choose two conditions away from the rotary resonances, with $\omega_{RF}/2\pi = 40$ kHz and two MAS rates of 60 and 200 kHz as well as one condition approaching the half-integer rotary resonance conditions with $\omega_{RF}/2\pi = 36$ kHz and $\omega_{MAS}/2\pi = 60$ kHz. Two cases of jump angles, 10° and 90°, are considered, with $p_1 = p_2 = 0.5$. As expected, the deviations between the two approaches are larger for the larger value of the jump angle as well as in the vicinity of the rotary resonances.[12] There is an additional source of deviations when $k_{ex} \approx C_q$, originating from the anisotropic loss of intensity due to the intermediate motional regime. Consequently, an expression based on the uniform averaging of the relaxation rates is inadequate in this case. When $k_{ex} \gg C_q$, the deviations between the two treatments are the least pronounced. Further, when $\omega_{MAS}/2\pi \gg C_q$ and for small-angle fluctuations the deviations become negligible for high values of spin-lock fields away from the rotary resonances, in agreement with homonuclear proton–proton rotating frame relaxation.[12] For deuterated methyl groups with a tensor magnitude of the order of 55 kHz, the condition $\omega_{MAS}/2\pi \gg C_q$ implies the necessity of spinning at a rate of about 200 kHz.

We now focus on the details of the relaxation rates behavior for large-angle jumps in different motional regimes and employ the Liouvillian approach in the subsequent simulations. Fig. 5A displays the simulated relaxation behavior for θ = 90° and a range of k_{ex} rates and several values of ω_{MAS} at a fixed value of the spin-lock field of 24 kHz. At conditions close to $\omega_{MAS} = \omega_{RF}, 2\omega_{RF}$ elevated relaxation rates are observed with broadened maxima, pointing to efficient relaxation, as expected qualitatively based on Eq. (2); here, the frequencies of the two major rotary resonance conditions, $\omega_{RF} = \frac{1}{2}\omega_{MAS}$ and $\omega_{RF} = \omega_{MAS}$, act as analogs of the conditions of $J(0)$. At higher values of ω_{MAS}, the relaxation rates fall and the maxima shift to higher values of k_{ex}. When $C_q \gg \omega_{MAS}$ (see the black line in Fig. 5A with $\omega_{MAS}/2\pi = 7$kHz), the qualitative picture of rotary resonance-driven maxima in the relaxation rates appears to break down.

Although in general the decay of magnetization during the spin-lock period is not expected to behave in a single-exponential fashion, the single-exponential approximation has been widely applied because of its ease of use. Examples of the magnetization decay curves at the maxima of relaxation rates (of Fig. 5A) are shown in Fig. 5B and 5C for the sum of all the side bands obtained for spin-lock times of 0 to 2 ms. The coherent oscillations are superimposed onto the decay due to motions and are especially apparent in the vicinity of the rotary resonances as expected. Due to these oscillations, we arbitrarily choose the "dead time" of the fits of 100 μs, as this likely corresponds to the minimal time at which the spin-lock can be established in most experimental conditions. In the theoretical simulations of Fig. 5 the sampling density is very high and the resulting relaxation times are practically independent of the choice of the dead time. The concept of dead time has been also used for fitting ^{15}N $R_{1\rho}$ relaxation data in proteins.[14] The duration is dependent on the system and extent of motions. The semilog plot emphasizes the deviations from the single-exponential approximation, which are apparent when the magnetization decays to 5% or below its initial value, justifying the use of the approximation. For low k_{ex} rates, a decay of magnetization below 5% may require long spin-lock times. In the experimental section, we provide a practical approach for dealing with incomplete decays when sampling time is limited by probe heating considerations.

Sensitivity to the exchange rate is shown in another way when we plot the simulated relaxation times $T_{1\rho} = 1/R_{1\rho}$ either as a function of MAS rate at a fixed value of the spin-locking field of 30 kHz (Fig. 6) or as a function of the spin-lock field strength at a fixed value of MAS rate of 60 kHz. As pointed out for spin ½ nuclei $R_{1\rho}$ relaxation,[5] the sensitivity of the k_{ex} rate constant is similar in the two approaches; however, from the experimental standpoint, it is easier to take the measurements in a controlled fashion by varying the RF field strength rather than the MAS rate.[5] Sensitivity to the value of k_{ex} is observed across the range shown. However, in the fast exchange limit, the dependence of the relaxation rate on either the MAS rate or the spin-lock field

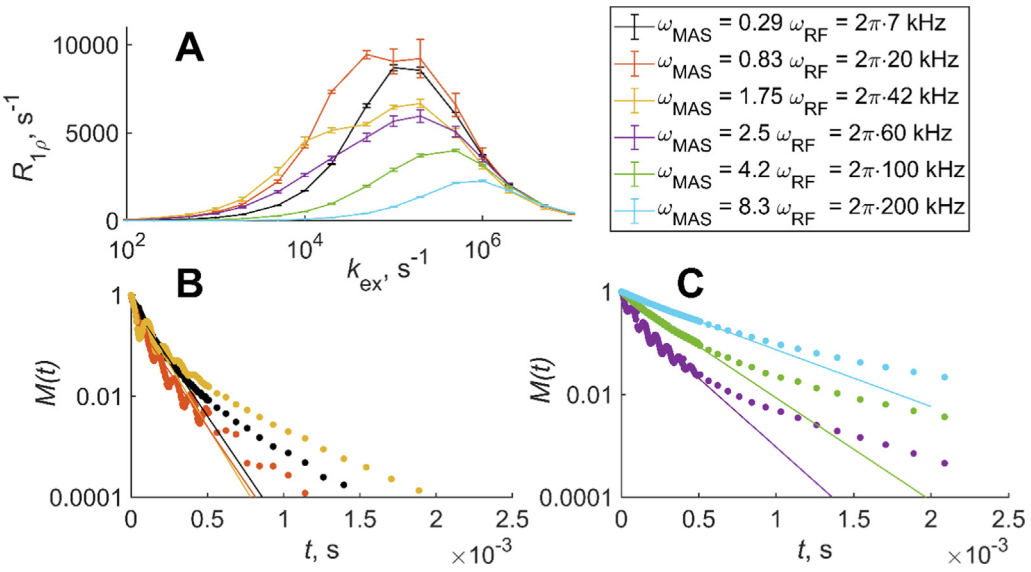

Fig. 5. A) ^{2}H relaxation rates $R_{1\rho}$ as a function of k_{ex} for $\omega_{RF}/2\pi$ of 24 kHz using the 2-site exchange model (Fig. 1C) with equal populations, $C_{q,1} = C_{q,2} = 55$ kHz, and $\theta = 90°$. The MAS rates and corresponding ω_{MAS}/ω_{RF} ratios are shown directly in the panels. The static magnetic field strength was taken as 17.6 T. The rates were obtained using the mono-exponential fits to the magnetization decay curves starting with the dead time of 100 μs. B) Examples of normalized magnetization decay curves $M(t)$ on the semilog scale for the maxima positions of part A). The solid lines represent mono-exponential fits starting with 100 μs dead time. Normalization was performed to the $t = 0$ value. Note the residual coherent oscillations in the vicinity of the rotary resonance conditions. The errors in the relaxation rate in Panel B were obtained using the inverse covariance matrix method.

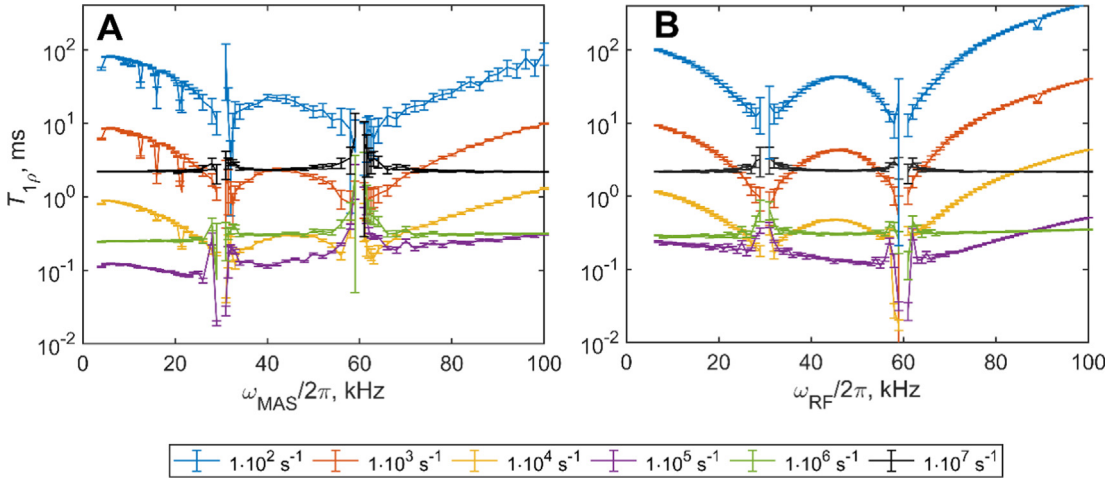

Fig. 6. Simulated ^{2}H $T_{1\rho}$ profiles (semilog scale) as a function of A) $\omega_{MAS}/2\pi$ with the fixed value of $\omega_{RF}/2\pi = 30$ kHz and B) $\omega_{RF}/2\pi$ with a fixed value of $\omega_{MAS}/2\pi = 60$ kHz for the 2-site exchange model (Fig. 1C) with equal populations, equal axially symmetric quadrupolar tensors in the two sites with $C_{q,1} = C_{q,2} = 55$ kHz, and the jump angle $\theta = 90°$. The different values of the conformational exchange rate constants k_{ex} are indicated directly in the panel legend. The relaxation times were obtained using a single-exponential function $M(t) = Ae^{-t/T_{1\rho}}$ with 52 spin-lock times in the 200 μs to 50 ms range, except for the limit of very slow relaxation for which additional large delays up to 5 s were included. The sampling of $\omega_{MAS}/2\pi$ in part A and $\omega_{RF}/2\pi$ in part B was performed with a step of 2 kHz, except in the vicinity of rotary resonances where the 1 kHz step was used. Powder averaging was performed with 1596 crystallite orientations and MAS evolution included at least 20 steps per rotor period. The static magnetic field strength was taken as 17.6 T.

strength disappears in accordance with the extreme narrowing limit. The $T_{1\rho}$ lines for the different k_{ex} rate constants can intersect, and the most direct way to resolve the ambiguity in the motional parameters is to measure the relaxation rates at either different spin-lock field strengths or different MAS conditions. It is preferable to perform these dispersion experiments outside the region of the half and full rotary resonance conditions, where dispersion behavior is non-monotonous, appears somewhat diminished, and can be partially masked by experimental errors. Additionally, as usual for dynamics studies, probing the temperature dependence of the motions is useful not only for resolving the ambiguities in the k_{ex} values but also for refining the motional mechanisms and determining the activation energies of the motional modes. While all the major rotary resonances ($n = 1$ or 2) are visible for all the k_{ex} rates, higher-order rotary resonances for $n > 2$ become less pronounced and are not visible for $k_{ex} > \omega_{MAS}$ due to the interference of motions with the coherent evolution. The rotary resonances remain visible for small values of k_{ex} (red and blue lines, Fig. 6A) at low MAS conditions. Fig. S3A displays an analog of simulations shown in Fig. 6B for small-angle fluctuations of 10°, with the qualitative features of the dispersion profiles remaining similar to those of the large-angle fluctuations. Fig. S3B focuses on the analog of Fig. 5A for the 10° amplitude fluctuations.

3.3. Results for DMS-D_6 validate the experimental and computational approaches

We now describe the experimental results for DMS-D_6. The situation is conceptually similar to the theoretical case of the 2-site exchange with large-angle jumps described above, with the important distinction of the addition of fast 3-site methyl jumps (Fig. 1A). In the theoretical case, the C_q values of 55 kHz corresponded to the fast averaging of methyl jumps, which has a non-averaged C_q value of 166 kHz for DMS.[31] However, in principle, the fast jump mode itself can contribute to the experimental relaxation rates. At low temperatures at which the large-angle fluctuations are too slow to have an appreciable effect on the relaxation, we observe dispersion profiles dominated by coherent oscillations, most pronounced in the vicinity of the rotary resonance conditions. Fig. S4 presents the experimental data at 277 K and a 25 kHz MAS rate. Away from the resonance conditions, the relaxation times obtained using the single-exponential approximation are consistent with those of the simulations performed using the corresponding 3-site jump rate constant (k_3) at these low temperatures. As elaborated above, in all our results, the *x*-axis is given by $\langle\omega_{RF}\rangle$, representing the average over the distributions of the spin-lock amplitudes (Fig. 2). Since the distributions themselves are highly asymmetric with a large left skew, the modal values of the spin-lock amplitudes are appreciably larger than the average values (1.5 times for the 1.3 mm probe and 1.25 times for the 2.5 mm probe). Thus, the rotary resonances shift to the apparent values $\langle\omega_{RF}\rangle$, which are effectively lower than those given by the $\frac{n}{2}\omega_{MAS}$ condition. The $R_{1\ \rho}$ relaxation data for DMS were collected at two MAS rates: the relatively low 10 kHz MAS rate that allows us to use spin-lock fields with magnitudes away from the rotary resonance conditions and the higher MAS rate of 60 kHz that is more suitable for samples for which site-specific resolution is desired. At the 10 kHz MAS rate, the main data were collected at a high temperature of 85 °C at which the flip motions are pronounced; however, at the 60 kHz MAS rate, we performed the experiments at 55 °C due to probe limitations. The static magnetic field was different in the two cases, however it has a minor effects on the rotating frame ^{2}H relaxation in the presence of slow motions which occur on the time scales much slower than the inverse of the Larmor frequency.

The partially relaxed spectra examples (i.e., spectra obtained as a result of rotating frame relaxation at a fixed value of the relaxation delay) obtained using the pulse sequence in Fig. 2A are shown in Fig. 7A. For the 10 kHz MAS rate, the major intensity concentrates at the first side bands at ± 10 kHz, and we thus used these side bands in the main analysis. At the 60 kHz MAS rate, most of the intensity is refocused into the central band. The residual coherent oscillations for small spin-lock fields (for the 10 kHz MAS rate) or those near rotary resonance conditions (for the 60 kHz MAS rate) are evident in the magnetization curves in Fig. 6B. Thus, the decay curves (Fig. 7B and Fig. S5) were sampled using 100 to 200 μs "dead times". The experimentally accessible length of the sampling of magnetization decay curves can be limited by probe duty cycle considerations and the sensitivity of the sample to RF-induced heating. For the 1.3 mm probe, we did not sample beyond 8 ms. With this upper limit on the sampling, the crystallite orientations with slower relaxation rates create an apparent baseline in some of the decay patterns. Fig. S6 shows an example of a histogram of simulated $R_{1\rho}$relaxation rates for individual crystallites of the powder pattern. For consistency, all the magnetization decay curves were thus fitted with the function $M(t) = Ae^{-t/T_{1\rho}} + B$. When limiting experimental sampling times, it is important to perform the simulations with the same spin-lock durations as used in the experiment in order not to artificially skew the simulated distributions compared with the experimental sampling. This approach thus emphasizes the faster relaxing components of the overall magnetization decay. One of alternative approaches would be to focus on the average relaxation rate over the distribution, given by $-\frac{1}{M(0)}\frac{dM}{dt}\big|_{t=0} \approx \frac{1}{T_{1\rho}}\frac{A}{A+B}$. The introduction of the baseline parameter is similar to the bi-exponential fit sometimes used in the fitting of ^{15}N MAS $R_{1\ \rho}$ decay curves[8]. The focus on the $T_{1\rho}$ parameter is, therefore, analogous to the selection of the fast relaxing component of the bi-exponential fitting function, especially for the situation when the slow-relaxing component is not well defined within the experimental precision. The fast and slow relaxing components were clearly visible in the static ^{2}H $R_{1\rho}$-measurements on DMS, for which the sampling time stretched to 50 ms.[23] It is in principle possible to obtain the selection of the model parameters by direct comparison of the experimental and simulated decay curves. However, the model parameters obtained this way will still depend on the exact choice of the relaxation delays, but the qualitative information encoded in the relaxation times will be lost. On the other hand, once the fits are obtained, it could be useful to cross-check the correspondence between the experimental decay curves and those obtained using the best-fit parameters (Fig. S7). The detailed analysis of the parametrization of the decay curves is presented in Fig. S8.

The resulting relaxation dispersion profiles (Fig. 8) demonstrate several distinct features. For the 10 kHz MAS rate, most of the employed spin-lock fields are higher than the first integer rotary resonance condition and a strong extent of the dispersion is observed at the high temperature of 85 °C. For the 60 kHz MAS rate and 55 °C, the dispersion is only observed for low values of ω_{RF}, as most of the ω_{RF} range falls between the first half-integer and full-integer resonance conditions. The RF inhomogeneity inclusion affects visual features of the dispersion profiles in comparison to the theoretical graphs. We next assess the sensitivity of the profiles to the k_{flip} rate constant and obtain the best-fitting values according to the model in Fig. 1A. The values of the k_3 rate constants for each temperature were obtained from the fits to the experimental longitudinal relaxation rates determined by the inversion recovery method at each temperature. The longitudinal relaxation times were 48 ms at 85 °C and the 10 kHz MAS rate and 26 ms at 55 °C and the 60 kHz MAS rate. For both MAS conditions, the profiles are sensitive to the value of k_{flip}, as shown in detail in Fig. S9 for the different side bands at the 10 kHz MAS rate and in Fig. S10 for the central band at the 60 kHz MAS rate. The best-fitting parameters (black bands in Fig. 8) are $k_{\text{flip}} = 3.5{\cdot}10^4$ s^{-1} for the 10 kHz MAS rate at 85 °C and $k_{\text{flip}} = 1.6{\cdot}10^3$ s^{-1} for the 60 kHz MAS rate at 55 °C. These values fall well within the ranges of parameters found in previous assessments of motions in DMS.[9,23,30–34] It appears that improving commercially available probes to minimize RF inhomogeneity factors would benefit these types of measurements.

The temperature dependence of the dynamics probes the details of the motional mechanisms and cross-validates the methodologies. Thus, we also assessed k_{flip} at different temperatures for DMS at a 10 kHz MAS rate. For this purpose, we applied a spin-lock field strength range well away from the first full major resonance and strong enough to ensure the sufficient locking of all the crystallite orientations, namely, 24 to 44 kHz. In the temperature range between 85 °C and 51 °C, the flipping motion is well pronounced and is expected to follow Arrhenius behavior with an activation energy range of 63 to 92 kJ/mol.[9,23,30–34] This range was determined by a variety of solid-state NMR techniques performed over different temperature ranges depending on the sensitivity of each technique. We have performed ^{2}H $R_{1\ \rho}$ measurements for five temperatures (Fig. 9A) and fitted the relaxation times of the first ±10 kHz side bands to the model in Fig. 1A. The

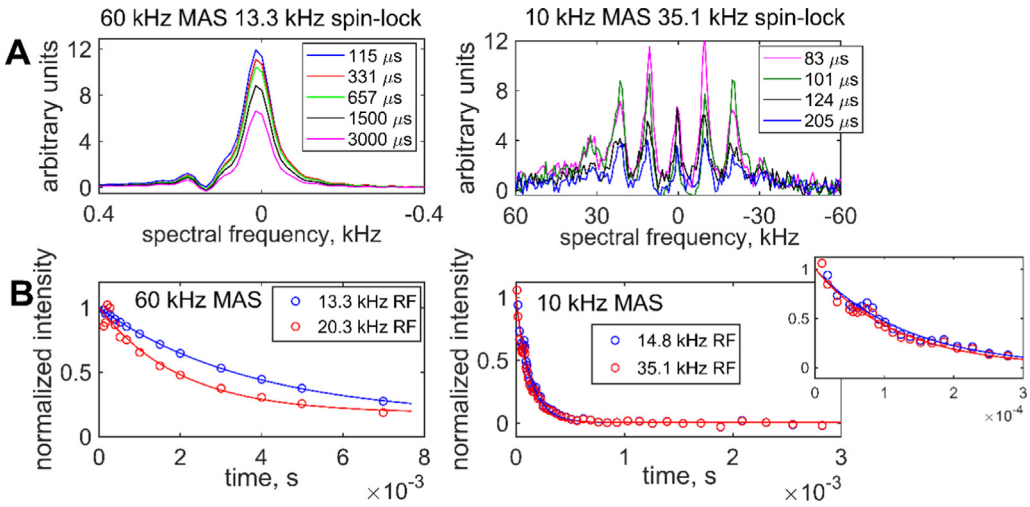

Fig. 7. A) Example of the partially relaxed spectra of DMS-D_6 for the $R_{1\,\rho}$ measurements at the 60 kHz MAS rate, 14.1 T, and 55 °C and the 10 kHz MAS rate, 17.6 T and 85 °C. The spin-lock strength and relaxation delay values are indicated directly in the panels. B) Examples of the magnetization decay curves for the 60 kHz MAS rate central band intensities and 10 kHz MAS rate first side-band intensities. The lines represent the fits to the mono-exponential function of the form $M(t) = Ae^{-t/T_{1\rho}} + B$. The insert for the 10 kHz MAS condition enlarges the initial magnetization decay curve time points to demonstrate the presence of the remaining coherent oscillations.

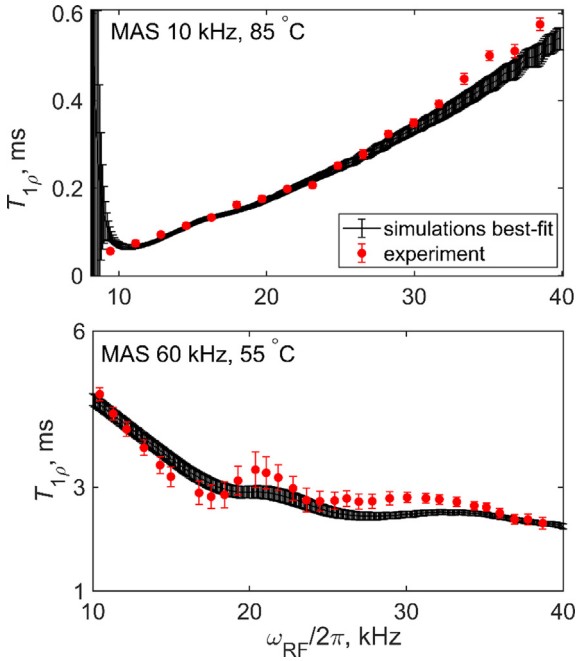

Fig. 8. $T_{1\,\rho}$ times *vs* $\omega_{RF}/2\pi$ in DSM-D_6 at the 10 kHz MAS rate, 17.6 T, and 85 °C for the first side bands at a ± 10 kHz spectral frequency (top panel) and at the 60 kHz MAS rate, 14.1 T, and 55 °C for the central band (bottom panel). The black bands represent the best-fit simulations according to the model in Fig. 1A with $k_3 = 5.7{\cdot}10^9$ s^{-1} and $k_{flip} = 3.5{\cdot}10^4$ s^{-1} for the 10 kHz MAS rate/85 °C data and $k_3 = 3.2{\cdot}10^9$ s^{-1} and $k_{flip} = 1.6{\cdot}10^3$ s^{-1} for the 60 kHz MAS rate/55 °C data. The effect of RF inhomogeneity with the inhomogeneity profiles in Fig. 2 was included in the simulations as described in the text and the reported $\omega_{RF}/2\pi$ values stand for the weighted averages over the distributions of the RF values. The error limits for both the experimental and the simulated values are obtained from the fits of the magnetization decay curves to the mono-exponential function of the form $M(t) = Ae^{-t/T_{1\rho}} + B$.

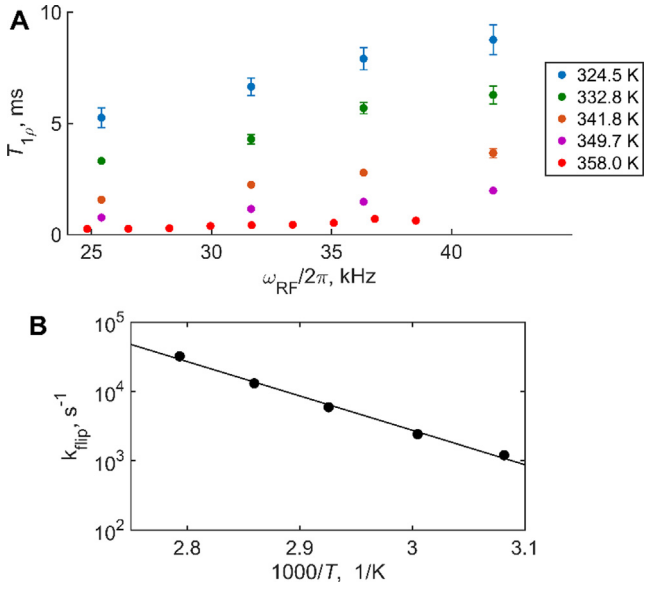

Fig. 9. A) $T_{1\,\rho}$ *vs* $\omega_{RF}/2\pi$ in DSM-D_6 obtained from the mono-exponential fits of the first side-band intensities, collected at the 10 kHz MAS rate and 17.6 T, with the temperatures indicated directly in the panel. The error bars smaller than the sizes of the symbols are not shown. B) Semilog plot of the fitted values of the k_{flip} rates for the $T_{1\rho}$ times shown in the top panel *vs* 1000/T. The resulting activation energy value is E_a = 94 ± 4 kJ/mol.

k_3 rate constants were fixed at values consistent with the T_1 measurements at each temperature (Table S1). The resulting Arrhenius plot (Fig. 9B) yields an activation energy E_a of 94 ± 4 kJ/mol, which is at the high end of the previously determined ranges. The Arrhenius prefactor ln$A$ is 42.1 ± 1.5, again falling in the upper range of the previously determined values, which is expected, as E_a and A have a positive correlation.

3.4. A β fibrils: An example of application to complex protein systems

We now assess the feasibility of the measurements for protein samples using the hydrated A $\beta_{1\text{-}40}$ fibrils labeled with a single methyl group at the A2 residue (Fig. 1B). Based on our previous measurements, the simplest model describing the dynamics of the disordered N-terminal domain is a two-site conformational exchange model with unequal populations.[27] The major state (referred to as the "free" state) has about a 92% population for the A2 residue and undergoes extensive large-scale rearrangements approximated as isotropic diffusion. These large-amplitude motions lead to a dramatic narrowing of the tensor, with an effective quadrupolar coupling constant of around 3 kHz.[27] By con-

trast, due to intra- and inter-molecular contacts, this diffusive motion is entirely quenched in the minor bound state, which retains the effective tensor typical of alanine methyl groups of 55 kHz. Because of the spectral dominance of the narrowed form (Fig. 10A) as well as the preference to employ low RF fields to avoid RF-induced heating and dehydration, an MAS rate of 8 kHz was chosen. With this MAS rate, a spin-lock field strength ranging between 10 and 27 kHz is sufficient for locking the major transverse component and this avoids the first half- and full-integer rotary resonance conditions. The magnetization decay curves (Fig. 10B, shown for the central band intensities) were sampled with nine points between 0.2 and 3.9 ms. The resulting relaxation dispersion profiles (Fig. 10C) indicate a moderate degree of dispersion. The fitting parameters of the motional model are the population of the bound state (p_{bound}), which was fixed at 8% based on the results of prior ^{2}H static line shape measurements,[27] the diffusion coefficient D for the large-scale rearrangement of the free state, and the conformational exchange rate constant k_{ex} between the two states. In principle, the population can be introduced as a free parameter; however, the three-variable parameter grid coupled with a long computational time is difficult to optimize. On our server, for each subset (p_{bound}, D, k_{ex}), the computational time for the $R_{1\,\rho}$ simulations under the full Liouvillian approach is 10 h without the inclusion of inhomogeneity modeling and 72 h with the inclusion of inhomogeneity modeling. Thus, a true full grid search was not feasible even for the (D, k_{ex}) space with a fixed value of p_{bound}. Alternative computational approaches can involve trajectory-based random walk methods.[52]

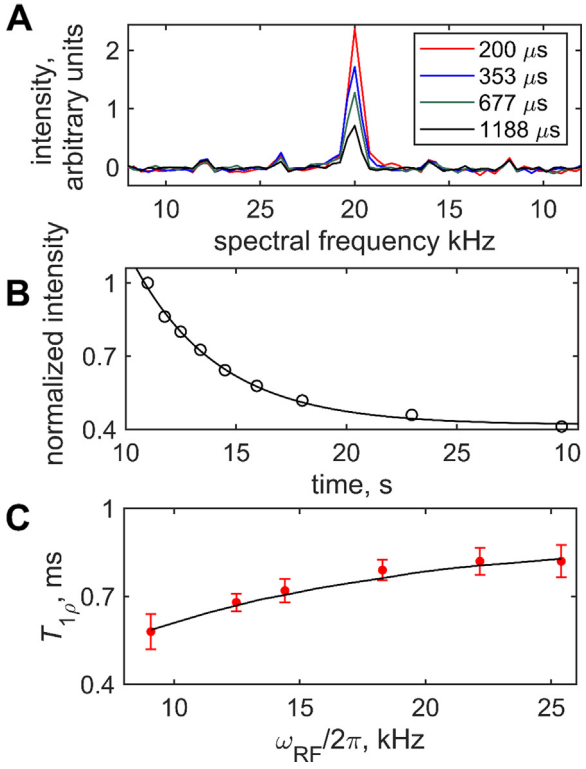

Fig. 10. Results of the $R_{1\,\rho}$ measurements for the A $\beta_{1\text{-}40}$ fibrils in the hydrated state and in the threefold symmetric polymorph, labeled at the A2-CD_3 site. The data were collected at an 8 kHz MAS rate, 17.6 T, and 37 °C. A) An example of partially relaxed spectra at $\omega_{RF}/2\pi$ = 22 kHz and relaxation delays indicated directly in the panel. The line-broadening function of 50 Hz was applied. B) Corresponding magnetization decay curve of the central band intensities. The line represents the fit to the mono-exponential function form $M(t) = Ae^{-t/T_{1\rho}} + B$. C) $T_{1\,\rho}$ times *vs* $\omega_{RF}/2\pi$ obtained from the mono-exponential fits of the central band. Uncertainties were obtained using the covariance matrix method. The line represents the best-fit according to the model in Fig. 1B with $D = 1.9{\cdot}10^6$ rad$^2{\cdot}$s^{-1}, $k_{ex} = 1{\cdot}10^5$ s^{-1}, and $p_{bound} = 0.08$.

We varied the values of D and k_{ex} around the wide subset of previously defined ranges for this system in an iterative manner to determine the best-fit set: the value of D was previously assessed to be in the range of 1.4 to $2.2{\cdot}10^6$ rad$^2{\cdot}$s^{-1} and k_{ex} dependence was analyzed to be between $1{\cdot}10^4$ and $2{\cdot}10^5$ s^{-1}. Both the values of the relaxation times and the extent/pattern of the dispersion profiles are clearly sensitive to the fitting parameters within these ranges (Fig. S11). The value of D has a major effect on the magnitude of $T_{1\,\rho}$, while k_{ex} variations have a more pronounced effect on the dispersion pattern. The best-fit set of simulations to the experimental $T_{1\,\rho}$ curve is $D = 1.9{\cdot}10^6$ rad$^2{\cdot}$s^{-1} and $k_{ex} = 1{\cdot}10^5$ s^{-1}, which is right within the range found by the ^{2}H MAS CEST measurements, for which the best-fitting parameters were $D = 1.9{\cdot}10^6$ rad$^2{\cdot}$s^{-1} and $k_{ex} = 0.2\text{–}1{\cdot}10^5$ s^{-1}.[45] The combination of static ^{2}H $R_{1\,\rho}$, quadrupolar CPMG relaxation, and static CEST data indicated the presence of multiple free states of the N-terminal domain in exchange with a single bound state.[24,26,27]. The ensemble is characterized by clusters of D values around $1\text{–}3{\cdot}10^6$ rad^2/s and $1{\cdot}10^8$ rad^2/s, with corresponding k_{ex} values clustered at $0.1\text{–}1{\cdot}10^5$ and $1\text{–}3{\cdot}10^6$ s^{-1}. Here, we constraint ourselves to the simple two-state model, as the current data and modeling grid are not sufficient to introduce a higher level of complexity. Nonetheless, the best-fitting parameters in this simplified model fall within one of these main clusters. The fact that we can match the data with the same set of parameters as previously determined from other techniques provide further confirmations of the model. This is especially important for the case of the fibrils, which clearly have a very complex dynamics in the disordered N-terminal domain.

A question remains whether the ^{2}H $R_{1\,\rho}$ rates would be sensitive to motional parameters at higher spinning speeds, which would be desirable if we probed the dynamics of the fibrils in a multiply labeled sample. While we have not performed the experiments under these conditions, we have simulated the relaxation rates at a 60 kHz MAS rate for the best-fitting parameters ($D = 1.9{\cdot}10^6$ rad$^2{\cdot}$s^{-1}, $k_{ex} = 1{\cdot}10^5$ s^{-1}) and a k_{ex} range of 0.5 to $2{\cdot}10^5$ s^{-1} (Fig. S12). We conclude that the measurements are expected to retain measurable sensitivity to the motional parameters and that the overall extent of dispersion is not reduced.

We expect the technique to be useful for a variety of biological systems from globular protein to amorphous aggregates. Identifying the best ways of motional modeling is the key for extracting meaningful information from these measurements. In cases when the validity of the Redfield approximation is expected, the so-called "model-free" approach may be appropriate and simplify the data analysis.[53]

4. Conclusion

Our results demonstrated the feasibility of the ^{2}H $R_{1\,\rho}$ relaxation technique under MAS conditions for studies of dynamics, particularly for protein methyl groups. Special care must be taken to select a range of MAS rates and spin-lock conditions that retain the sensitivity of the quadrupolar tensor reorientations to motions. When selecting these conditions, one has to be aware of the rotary resonances at $\omega_{RF} = \frac{n}{2}\omega_{MAS}$ that are often significantly broadened due to the RF inhomogeneity factors of the coil. The RF inhomogeneity needs to be assessed and included explicitly in the simulations if its contribution is significant. The durations of spin-lock times are often limited by probe safety limits and/or sample tolerance to RF-induced heating. When the sampling window is limited, it is important to conduct simulations with spin-lock times matching those of the experiment.

In our modeling approach, we provided examples of explicit motional modeling, which allows for confirmation of motional mechanisms and its parameters. In particular, for DMS a relatively simple 2-site rotameric exchange model and known ranges of parameters across the 85–51 °C temperature range were confirmed. For the A2-CD_3 methyl group in the disordered domain of amyloid- β fibrils, the results confirmed the large-scale fast diffusive motions of the N-terminal domain coupled with a slow conformational exchange between the free and bound states of the domain at $k_{ex} = 1 \cdot 10^5\ s^{-1}$. Large magnitudes of quadrupolar tensors in general preclude analytical Redfield treatment for MAS rates less than or comparable to the quadrupolar coupling constant, especially for large-angle fluctuations that are typical of rotameric interconversions. Instead, a numerical integration of the Liouville–von Newman equation is suggested for the computation. These computations can be time consuming and require optimization of computational strategies and computer hardware.

The rotating frame deuterium relaxation data are well suited for the assessment and confirmation of the motional mechanisms, particularly for the large-angle fluctuations of protein side-chains. It is also complementary to other solid-state NMR techniques such as laboratory frame relaxation focused on faster time scales, line shape analysis, and Q-CEST measurements. The latter in principle has the capacity to probe even slower time scales in the slow motional regime with respect to the effective field. [22,24,45] Possible extensions of the approach include a) off-resonance measurement to increase the range of effective fields available and thus access a wider range of time scales without adding RF-induced heating; and b) coupling ^2H $R_{1\ \rho}$ measurements to ^{13}C polarization transfer approaches [28,54] to enable site-specific resolution in a two-dimensional fashion for multiply labeled protein samples. These extensions may require the use of adiabatic full passage pulses for the optimization of the cross-polarization conditions as well as adiabatic ramp pulses for the alignment of the magnetization along the effective field for the off-resonance irradiation.[55,56] In terms of applications, the technique is not limited to methyl groups but can encompass a range of side chain reorientation dynamics such as phenylalanine, histidine, and proline rings as well as polar side chain sites.

Declaration of Competing Interest

The authors declare that they have no known competing financial interests or personal relationships that could have appeared to influence the work reported in this paper.

Acknowledgements

This work was supported by a National Institutes of Health Grant (1R15-GM111681). Several experiments were performed at the National High Magnetic Field Laboratory, which is supported by NSF Cooperative Agreement NSF/DMR-1644779, the State of Florida, and the U.S. Department of Energy.

Appendix A. Supplementary material

Supplementary data to this article can be found online at https://doi.org/10.1016/j.jmr.2022.107171.

References

[1] D.D. Boehr, R. Nussinov, P.E. Wright, The role of dynamic conformational ensembles in biomolecular recognition, Nat. Chem. Biol. 5 (2009) 789–796.
[2] P. Schanda, M. Ernst, Studying dynamics by magic-angle spinning solid-state NMR Spectroscopy: principles and applications to biomolecules, Prog. Nucl. Magn. Reson. Spectrosc. 96 (2016) 1–46.
[3] A.G. Palmer 3rd, Chemical exchange in biomacromolecules: past, present, and future, J. Magn. Reson. 241 (2014) 3–17.
[4] N.-A. Lakomek, S. Penzel, A. Lends, R. Cadalbert, M. Ernst, B. Meier, Microsecond dynamics in ubiquitin probed by solid-state NMR 15N R1rho relaxation experiments under fast MAS (60–110 kHz), Chemistry 23 (2017) 9425–9433.
[5] A. Krushelnitsky, T. Zinkevich, B. Reif, K. Saalwächter, Slow motions in microcrystalline proteins as observed by MAS-dependent 15N rotating-frame NMR relaxation, J. Magn. Reson. 248 (2014) 8–12.
[6] V. Kurauskas, S.A. Izmailov, O.N. Rogacheva, A. Hessel, I. Ayala, J. Woodhouse, A. Shilova, Y. Xue, T. Yuwen, N. Coquelle, J.-P. Colletier, N.R. Skrynnikov, P. Schanda, Slow conformational exchange and overall rocking motion in ubiquitin protein crystals, Nat. Commun. 8 (2017) 145.
[7] C. Quinn, A. McDermott, Monitoring conformational dynamics with solid-state R1qexperiments, J. Biomol. NMR 45 (2009) 5–8.
[8] P. Ma, J.D. Haller, J. Zajakala, P. Macek, A.C. Sivertsen, D. Willbold, J. Boisbouvier, P. Schanda, Probing Transient Conformational States of Proteins by Solid-State R(1ρ) Relaxation-Dispersion NMR Spectroscopy, Angew. Chem. (Int. Ed.) 53 (2014) 4312–4317.
[9] C.M. Quinn, A.E. McDermott, Quantifying conformational dynamics using solid-state R1ρ experiments, J. Biomol. NMR 222 (2012) 1–7.
[10] D.F. Gauto, A. Hessel, P. Rovó, V. Kurauskas, R. Linser, P. Schanda, Protein conformational dynamics studied by 15N and 1H R1ρ relaxation dispersion: Application to wild-type and G53A ubiquitin crystals, Solid State Nucl. Magn. Reson. 87 (2017) 86–95.
[11] P. Rovó, R. Linser, Microsecond timescale protein dynamics: a combined solid-state NMR approach, ChemPhysChem 19 (2018) 34–39.
[12] P. Rovó, R. Linser, Microsecond time scale proton rotating-frame relaxation under magic angle spinning, J. Phys. Chem. B 121 (2017) 6117–6130.
[13] D. Marion, D.F. Gauto, I. Ayala, K. Giandoreggio-Barranco, P. Schanda, Microsecond protein dynamics from combined Bloch-McConnell and Near-Rotary-Resonance R(1ρ) relaxation-dispersion MAS NMR, ChemPhysChem 20 (2019) 276–284.
[14] A. Krushelnitsky, D. Gauto, D.C. Rodriguez Camargo, P. Schanda, K. Saalwachter, Microsecond motions probed by near-rotary-resonance R1rho (15)N MAS NMR experiments: the model case of protein overall-rocking in crystals, J. Biomol. NMR 71 (2018) 53–67.
[15] P. Rovó, Recent advances in solid-state relaxation dispersion techniques, Solid State Nucl. Magn. Reson. 101665 (2020).
[16] P. Schanda, Relaxing with liquids and solids - A perspective on biomolecular dynamics, J. Magnet. Resonance (San Diego Calif.:1997) 306 (2019) 180–186.
[17] P. Rovó, C.A. Smith, D. Gauto, B.L. de Groot, P. Schanda, R. Linser, Mechanistic insights into microsecond time-scale motion of solid proteins using complementary 15N and 1H relaxation dispersion techniques, J. Am. Chem. Soc. 141 (2019) 858–869.
[18] A.V. Struts, G.F.J. Salgado, K. Martnez-Mayorga, M.F. Brown, Retinal dynamics underlie its switch from inverse agonist to agonist during rhodopsin activation, Natur. Struct. Mol. Biol. 18 (2011) 392–394.
[19] C. Sun, O. Mitchell, J.X. Huang, G.S. Boutis, NMR studies of localized water and protein backbone dynamics in mechanically strained elastin, J. Phys. Chem. B 115 (2011) 13935–13942.
[20] R.L. Vold, R.R. Vold, Deuterium Relaxation in Molecular Solids, in: W. Warren (Ed.), Advances in Magnetic and Optical Resonance, Academic Press, San Diego, 1991, pp. 85–171.
[21] L. Vugmeyster, D. Ostrovsky, Static solid-state 2H NMR methods in studies of protein side-chain dynamics, Prog. Nucl. Magn. Reson. Spec. 101 (2017) 1–17.
[22] L. Vugmeyster, Recent developments in deuterium solid-state NMR for the detection of slow motions in proteins, Solid State Nucl. Magn. Reson. 111 (2021) 101710.
[23] L. Vugmeyster, D. Ostrovsky, Deuterium rotating frame NMR relaxation measurements in the solid state under static conditions for quantification of dynamics, ChemPhysChem 20 (2019) 333–342.
[24] L. Vugmeyster, D. Ostrovsky, R. Fu, Deuteron quadrupolar chemical exchange saturation transfer (Q-CEST) solid-state NMR for static powder samples: approach and applications to amyloid-β fibrils, ChemPhysChem 21 (2020) 220–231.
[25] L. Vugmeyster, D.F. Au, D. Ostrovsky, B. Kierl, R. Fu, Z.W. Hu, W. Qiang, Effect of post-translational modifications and mutations on amyloid-beta fibrils dynamics at N terminus, Biophys. J. 117 (2019) 1524–1535.
[26] L. Vugmeyster, D.F. Au, D. Ostrovsky, R. Fu, Deuteron solid-state NMR relaxation measurements reveal two distinct onformational exchange processes in the disordered N-terminal domain of amyloid-b fibrils, ChemPhysChem 20 (2019) 1680.
[27] D.F. Au, D. Ostrovsky, R. Fu, L. Vugmeyster, Solid-state NMR reveals a comprehensive view of the dynamics of the flexible, disordered N-terminal domain of amyloid-β fibrils, J. Biol. Chem. 294 (2019) 5840–5853.
[28] Ü. Akbey, Dynamics of uniformly labelled solid proteins between 100 and 300 K: A 2D (2)H-(13)C MAS NMR approach, J. MAgn. Reson. (San Diego, Calif.: 1997), 327 (2021) 106974.
[29] F.H. Larsen, H.J. Jakobsen, P.D. Ellis, N.C. Nielsen, Sensitivity-enhanced quadrupolar-echo NMR of half-integer quadrupolar nuclei. Magnitudes and relative orientation of chemical shielding and quadrupolar coupling tensors, J. Phys. Chem. A 101 (1997) 8597–8606.
[30] J.D. Cutnell, W. Venable, Nonexponential nuclear spin-lattice relaxation in polycrystalline dimethyl sulfone, J. Chem. Phys. 60 (1974) 3795–3801.

[31] M.J. Brown, R.L. Vold, G.L. Hoatson, Selective inversion investigations of slow molecular motion in solid state deuteron NMR spectroscopy, Solid State Nucl. Magn. Reson. 6 (1996) 167–185.
[32] C. Quinn, A. McDermott, Monitoring conformational dynamics with solid-state R1q experiments, J. Biomol. NMR 45 (2009) 5–8.
[33] D.E. Favre, D.J. Schaefer, B.F. Chmelka, Direct determination of motional correlation times by 1D MAS and 2D exchange NMR techniques, J. Magn. Reson. A 134 (1998) 261–279.
[34] L. Frydman, S. Vallabhaneni, Y.K. Lee, L. Emsley, Solid-state dynamic processes in complex systems analyzed by two-dimensional isotropic–anisotropic correlation nuclear magnetic resonance, J. Chem. Phys. 101 (1994) 111–117.
[35] A.K. Paravastu, A.T. Petkova, R. Tycko, Polymorphic fibril formation by residues 10–40 of the Alzheimer's β-Amyloid peptide, Biophys. J. 90 (2006) 4618–4629.
[36] A.T. Petkova, R.D. Leapman, Z.H. Guo, W.M. Yau, M.P. Mattson, R. Tycko, Self-propagating, molecular-level polymorphism in Alzheimer's beta-amyloid fibrils, Science 307 (2005) 262–265.
[37] K. Brannstrom, A. Ohman, L. Nilsson, M. Pihl, L. Sandblad, A. Olofsson, The N-terminal region of amyloid beta controls the aggregation rate and fibril stability at low pH through a gain of function mechanism, J. Am. Chem. Soc. 136 (2014) 10956–10964.
[38] H.A. Scheidt, I. Morgado, S. Rothemund, D. Huster, Dynamics of amyloid beta fibrils revealed by solid-state NMR, J. Biol. Chem. 287 (2012) 2017–2021.
[39] A.T. Petkova, W.M. Yau, R. Tycko, Experimental constraints on quaternary structure in Alzheimer's beta-amyloid fibrils, Biochemistry 45 (2006) 498–512.
[40] I. Bertini, L. Gonnelli, C. Luchinat, J. Mao, A. Nesi, A New structural model of A beta(40) fibrils, J. Am. Chem. Soc. 133 (2011) 16013–16022.
[41] A. Olofsson, A.E. Sauer-Eriksson, A. Ohman, The solvent protection of Alzheimer amyloid-beta-(1–42) fibrils as determined by solution NMR spectroscopy, J. Biol. Chem. 281 (2006) 477–483.
[42] S.K. Zaremba, Good lattice points, discrepancy, and numerical integration, Ann. di Mat. Pura ed Appl. 73 (1966) 293–317.
[43] V.B. Cheng, H.H. Suzukawa, M. Wolfsberg, Investigations of a nonrandom numerical method for multidimensional integration, J. Chem. Phys. 59 (1973) 3992–3999.
[44] P.-O. Persson, G. Strang, A Simple Mesh Generator in MATLAB, SIAM Rev. 46 (2004) 329–345.
[45] L. Vugmeyster, D. Ostrovsky, A. Greenwood, R. Fu, DeuteroncChemical exchange saturation transfer for the detection of slow motions in rotating solids, Front. Mol. Biosci. 8 (2021).
[46] A.J. Vega, MAS NMR spin locking of half-integer quadrupolar nuclei, J. Magn. Reson. 96 (1992) 50–68.
[47] R.L. Vold, G.L. Hoatson, L. Vugmeyster, D. Ostrovsky, P.J. De Castro, Solid state deuteron relaxation time anisotropy measured with multiple echo acquisition, Phys. Chem. Chem. Phys. 11 (2009) 7008–7012.
[48] R. Gupta, G. Hou, T. Polenova, A.J. Vega, RF inhomogeneity and how it controls CPMAS, Solid State Nucl Magn. Reson. 72 (2015) 17–26.
[49] N.C. Nielsen, H. Bildso/e, H.J. Jakobsen, M.H. Levitt, Double-quantum homonuclear rotary resonance: Efficient dipolar recovery in magic-angle spinning nuclear magnetic resonance, J. Chem. Phys., 101 (1994) 1805-1812.
[50] R. Kurbanov, T. Zinkevich, A. Krushelnitsky, The nuclear magnetic resonance relaxation data analysis in solids: General R1/R1ρ equations and the model-free approach, J. Chem. Phys. 135 (2011) 184104.
[51] D.A. Torchia, A. Szabo, Spin-lattice relaxation in solids, J. Magn. Reson. 49 (1982) 107–121.
[52] A. Krushelnitsky, G. Hempel, Y. Golitsyn, A. Wurl, K. Saalwächter, D. Reichert, Trajectory-based approach for the analysis of CODEX solid-state exchange experiments in the slow and intermediate motion regime: comparison of experiment, simulation, and analytical treatment, J. Phys. Chem. C. 125 (2021) 6839–6850.
[53] G. Lipari, A. Szabo, Model-Free approach to the interpretation of nuclear magnetic-resonance relaxation in macromolecules. 1. Theory and range of validity, J. Am. Chem. Soc. 104 (1982) 4546–4559.
[54] S.K. Jain, A.B. Nielsen, M. Hiller, L. Handel, M. Ernst, H. Oschkinat, U. Akbey, N.C. Nielsen, Low-power polarization transfer between deuterons and spin-1/2 nuclei using adiabatic (CP)-C-RESPIRATION in solid-state NMR, Phys. Chem. Chem. Phys. 16 (2014) 2827–2830.
[55] S. Wi, R.W. Schurko, L. Frydman, Broadband adiabatic inversion cross-polarization phenomena in the NMR of rotating solids, Solid State Nucl. Magn. Reson. 94 (2018) 31–53.
[56] F.A.A. Mulder, R.A. de Graaf, R. Kaptein, R. Boelens, An off-resonance rotating frame relaxation experiment for the investigation of macromolecular dynamics using adiabatic rotations, J. Magn. Reson. 131 (1998) 351–357.